

# The impact of wind corrections and ocean-current influence on wind stress forcing on the modeling of Pacific North Equatorial Countercurrent

Zhikuo Sun <sup>a,b,\*</sup>, Justin Small <sup>c</sup>, Frank Bryan <sup>c</sup>, Yu-heng Tseng <sup>d</sup>, Hailong Liu <sup>b,e</sup>, Pengfei Lin <sup>b,e</sup>

<sup>a</sup> School of Atmospheric Sciences, Sun Yat-sen University (SYSU), and Southern Marine Science and Engineering Guangdong Laboratory (Zhuhai), Zhuhai, China

<sup>b</sup> State Key Laboratory of Numerical Modeling for Atmospheric Sciences and Geophysical Fluid Dynamics (LASG), Institute of Atmospheric Physics, Chinese Academy of Sciences, Beijing, 100029, China

<sup>c</sup> National Center for Atmospheric Research (NCAR), Boulder, CO, 80301, USA

<sup>d</sup> Institute of Oceanography, National Taiwan University, Taipei, 10650, Taiwan

<sup>e</sup> College of Earth and Planetary Sciences, University of Chinese Academy of Sciences, Beijing 100049, China

## ARTICLE INFO

### Keywords:

Pacific North Equatorial Countercurrent

Wind correction

Double-counting bias

## ABSTRACT

Bias correction of reanalysis-based wind stress using scatterometer derived equivalent neutral wind has been a common practice in producing the forcing datasets used in recent global ocean model intercomparisons (OMIPs). Here we systematically evaluate the effect of this wind correction procedure on the simulation of the Pacific North Equatorial Countercurrent (NECC) with multiple sets of model experiments. The weak NECC evident in earlier OMIPs employing the Coordinated Ocean-ice Reference Experiments (COREs) forcing dataset persists with the new JRA55-do (Japanese 55-year Reanalysis) forcing dataset. Two factors appear to significantly affect the Pacific NECC in forced ocean simulations: i) the bias correction procedure using QuikSCAT derived winds and ii) whether or not the ocean current is considered in the bulk formula. In the forced ocean simulations, the QuikSCAT correction weakens the averaged NECC transports by about 60%. Taking the ocean currents into account in the bulk formula may weaken the averaged NECC transports by about 26%–30%. Under the current OMIP protocol the above two procedures are used together to force the ocean model resulting in a double-counting of ocean surface current feedback on wind stress because the QuikSCAT estimates the equivalent 10-m neutral winds relative to surface current. We further systematically verify and investigate the impacts of this double-counting of the ocean surface currents on the modeled Pacific NECC using offline linear Sverdrup transport analysis, in which the observational data of vector wind and surface current are used to calculate the surface wind stress. It shows that including the ocean current in the bulk formula may reduce the zonal Sverdrup transport (ZST) by about 6.6 Sv (33%) and the further double-counting of the ocean current leads to an additional reduction of 6.4 Sv (48%). Next, using “perfect model” experiments with output from a coupled ocean–atmosphere model we further identify that the double-counting of current feedback in the bulk formula results in approximately 21% weakened volume transport. The built-in nonlinear processes in the model, such as the advection and friction terms, may partly damp the reduction due to the double-counting of the ocean current. However, the double-counting bias can only explain 26%–30% of the Pacific NECC simulation bias and the other part of the bias, around 30%, caused by the correction with QuikSCAT has not been explained. We speculate that this part may be explained by the retrieval biases in QuikSCAT wind data and the use of annual mean climatological wind adjustment factors.

## 1. Introduction

The North Equatorial Countercurrent (NECC) is an eastward upper-ocean wind-driven current, located between 3° and 10°N in the tropical Pacific Ocean (Wyrtki and Kendall, 1967; Donguy and Meyers, 1996; Johnson et al., 2002). The NECC transports a significant amount (about 10~30 Sv) of water out of the western Pacific warm pool region to the relatively cold eastern Pacific. It plays an important role in maintaining

the warm pool heat budget (Meyers and Donguy, 1984; Picaut and Delcroix, 1995; Clement et al., 2005; Chen et al., 2016) so as to modulate the tropical Pacific climate (Richards et al., 2009; Masunaga and L'Ecuyer, 2011; Tan and Zhou, 2018).

The simulated NECC in the stand-alone ocean models participating in the second phase of the Coordinated Ocean-ice Reference Experiments (CORE-II) seems to be generally weak (Tseng et al., 2016,

\* Corresponding author at: School of Atmospheric Sciences, Sun Yat-sen University (SYSU), and Southern Marine Science and Engineering Guangdong Laboratory (Zhuhai), Zhuhai, China.

E-mail address: [sunzhikuo14@mails.ucas.ac.cn](mailto:sunzhikuo14@mails.ucas.ac.cn) (Z. Sun).

their Figure 19). The mean zonal currents of the NECC at 140°W in all 15 participating models is weaker than the observational value from Johnson et al. (2002) for the same time period. This bias may potentially affect the simulated upper tropical Pacific climatology and its seasonal and interannual variability. Sun et al. (2019) suggested that the simulated NECC biases are primarily due to the biases in the zonal surface wind stress and wind stress curl (WSC) (Wu et al., 2012), introduced by the satellite (QuikSCAT) based wind bias correction of the reanalysis surface wind. A similar correction was also applied in the new forcing dataset, JRA55-do (Japanese 55-year reanalysis data for driving ocean-sea ice models, Tsujino et al., 2018) used in the recent Ocean Model Intercomparison Program phase 2 (OMIP). Thus, the next generation of forced ocean-sea ice model experiments may potentially suffer from similar biases in the tropical Pacific and it is necessary to investigate the fundamental causes, so as to improve the existing wind correction procedure. Recent results from the OMIP-2 do show a weak NECC, though slightly stronger than that for OMIP-1 forced by the CORE-II forcing (Tsujino et al., 2020, Figure S44 for OMIP-1 and S45 for OMIP-2). The reanalysis dataset has its own bias and it is necessary to be corrected with scatterometer observations in order to improve the forcing wind field and the model results (Tsujino et al., 2018; Belmonte Rivas and Stoffelen, 2019), but from the point of view of NECC simulation, the QuikSCAT correction makes things worse.

The typical procedure used to correct 10 m reanalysis winds (such as JRA-55) with QuikSCAT in a standard OMIP experiment is provided in Fig. 1. The surface wind stresses,  $\vec{\tau}$ , are derived from the bulk formula. The magnitude and direction of the uncorrected reanalysis wind vector are adjusted by an offsetting factor  $\Delta W(\lambda, \phi)$  and a counter-clockwise rotating factor  $\chi(\lambda, \phi)$ , respectively, where  $\lambda$  and  $\phi$  are longitude and latitude, respectively. These offsetting factors are computed in three phases: 1958–1972, 1973–1997 and 1998–present, according to reference data: the microwave scatterometer (QuikSCAT) and radiometer (SSM/I) (Table 6 in Tsujino et al., 2018). The first two periods (1958–1972 and 1973–1997) are corrected using the Remote Sensing Systems SSM/I wind speed data and the third period is corrected using the QuikSCAT wind vector data. The Remote Sensing Systems SSM/I wind was also adjusted relative to QuikSCAT in Nov 1999–Oct 2009 (Tsujino et al., 2018). Therefore, our discussion focuses on the third period, during which the correction is directly related to QuikSCAT. Here, we address how the ocean currents and atmosphere winds are fed through the coupler and, for simplicity, we are ignoring other variables (10 m air temperature, 10 m specific humidity, SST etc.) in the flux computations which may also affect drag coefficient in Fig. 1.

As described in Tsujino et al. (2018), the Remote Sensing Systems QuikSCAT Ku-2011 Daily Ocean Vector Winds on 0.25 deg grid version 4 (QuikSCAT v.4) (Ricciardulli and Wentz, 2015) was used to correct the wind field of JRA55-raw dataset and the atmospheric stability is the only factor considered when inverting QuikSCAT v.4 wind field with empirically derived geophysical model function (GMF). Although de Kloe et al. (2017) further considered air density in the process of inversion to improve the use of scatterometer measurements and make scatterometer winds best represented by so-called stress-equivalent 10-m winds, the Remote Sensing Systems QuikSCAT product only estimates the equivalent 10 m neutral winds ( $\vec{U}_{10n}$ , Liu and Tang, 1996; Wentz and Smith, 1999; Chelton et al., 2001) and corresponding surface stresses (Liu and Tang, 1996; Kelly et al., 2001). Therefore, two possible sources of errors exist when the reanalysis actual 10 m winds are corrected towards the QuikSCAT  $\vec{U}_{10n}$ . First, in the regions of an unstable air-sea interface, the neutral winds,  $\vec{U}_{10n}$ , are stronger than the actual winds, typically by a few tens of  $\text{cm s}^{-1}$  (Liu and Tang, 1996). Thus, by adjusting the actual winds in the reanalysis towards the QuikSCAT  $\vec{U}_{10n}$ , the wind speed is spuriously increased in these unstable regions; particularly in the tropics (e.g., Warm Pool) and western boundary currents in winter. This potential source of error has already been taken into account in the new OMIP dataset (Tsujino et al., 2018), in which the 10 m actual winds in JRA55 reanalysis are

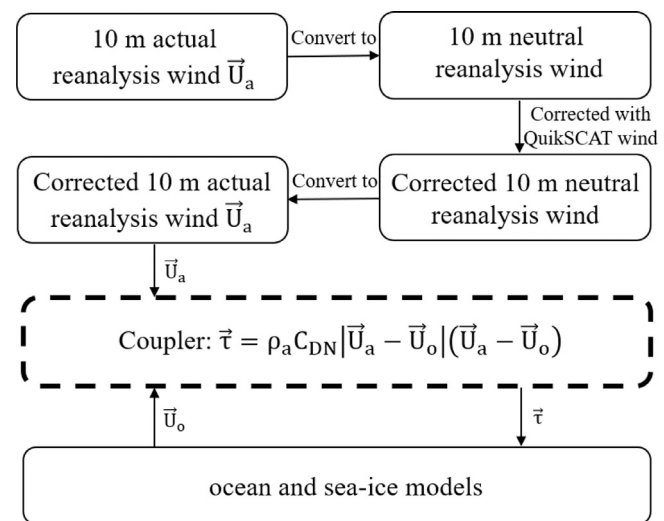


Fig. 1. The typical procedure to use 10 m reanalysis winds with the QuikSCAT correction in a standard JRA-55 experiment. The bulk formula is used to calculate the surface wind stress ( $\vec{\tau}$ ).  $\rho_a$ ,  $C_{DN}$ ,  $\vec{U}_a$ ,  $\vec{U}_o$  are atmosphere density, the neutral 10 m drag coefficient, the 10 m wind vector and the surface ocean current, respectively.

converted to  $\vec{U}_{10n}$  before performing the wind correction. After the wind correction, the results are converted back to 10 m actual winds again to force the sea-ice ocean models (Fig. 1).

Second, the QuikSCAT surface winds  $\vec{U}_{10n}$  are a function of the air-sea motion difference, i.e., the relative wind (Kelly et al., 2001; Chelton et al., 2004). The surface currents simulated by ocean models are usually fed into the surface bulk flux calculations to ensure the physical integrity of the atmosphere-ocean coupling when dealing with forced ocean models (Cornillon and Park, 2002; Kelly et al., 2001; Large and Yeager, 2004; Hersbach and Bidlot, 2008; Belmonte Rivas and Stoffelen, 2019). That is, the effect of surface currents has already been taken into account in the flux algorithm through  $(\vec{U}_a - \vec{U}_o)$ , where  $\vec{U}_a$  is 10 m actual wind and  $\vec{U}_o$  is ocean surface current. Therefore, if the QuikSCAT data is directly used to correct the reanalysis 10 m winds, the impact of ocean surface current on the surface stress may be counted twice. Because the zonal surface winds are against the surface currents in the NECC region on average, the easterly trade winds will be spuriously enhanced, leading to the change of WSC on both sides of Pacific NECC, which can then affect the simulation of NECC. Tsujino et al. (2018) and Renault et al. (2020) have previously recognized the double counting effect of the current feedback to the atmosphere when forcing oceanic simulations. However, Tsujino et al. (2018) only gave a qualitative description of above-mentioned double counting bias and Renault et al. (2020) mainly focused on the overall simulation of large-scale circulation and mesoscale eddies between 45°S and 45°N, not specifically in the NECC region. The specific comparison between their research and ours will be expanded in the discussion part.

The objective of the present paper is to evaluate the impact of satellite-based wind corrections to the JRA55 dataset on the simulation of the NECC in ocean models. Specifically, we investigate the impact of possibly double-counting the influence of ocean currents in stress, using numerical models and diagnostics. Other possible error sources introduced by QuikSCAT wind correction are also discussed.

## 2. Datasets, numerical experiments and methods

### 2.1. OMIP-2 forcing and observation datasets

JRA-55 is an atmospheric reanalysis dataset on the reduced TL319 (~55 km) grid, available from 1958 to present with 3h temporal resolution. The current feedback (CFB) in the momentum coupling

between ocean and atmosphere is not considered (JMA, 2013; O'Neill et al., 2015). To derive an appropriate forcing dataset for OMIP-2, the original JRA-55 dataset has been adjusted (see details in Tsujino et al., 2018), which is called JRA55-do. The atmospheric variables provided with the dataset include: 10 m wind vector ( $\vec{U}_a$ ), 10 m specific humidity, 10 m air temperature, sea level pressure, precipitation, snow, downward shortwave, downward longwave radiation and river runoff. We use two versions of the JRA55-do data in the present study: JRA55-do-v1.1 (downloadable from <http://amaterasu.ees.hokudai.ac.jp/~tsujino/JRA55-do-v1.1/>) and JRA55-do-v1.3 (downloadable from <http://amaterasu.ees.hokudai.ac.jp/~tsujino/JRA55-do-v1.3/>). The plan of Tsujino et al. is to continually update its version using near real-time updates to the raw JRA55 reanalysis, and the version number of JRA55-do dataset will advance whenever new datasets or adjustment methods are incorporated. Version 1.3 is evolved from the version 1.1 and 1.2 with some changes to the wind field. From version 1.1 to version 1.2, an error in computing the annual mean climatology of wind speed for JRA55-do and a subset of JRA55-do was corrected. It resulted in minor (less than 0.5%) changes in the wind speed adjustment factors. From version 1.2 to version 1.3, the same adjustment procedure is applied for the wind direction, while minor differences exist in the wind speed adjustment. The magnitude of the wind vector was adjusted by a multiplicative factor in version 1.2, whereas an offsetting factor was used for version 1.3 (Tsujino et al., 2018). The variables from the unadjusted JRA55 data, called JRA-raw here, are also used in this study.

To evaluate the model results, we use in situ observations of ocean currents (Johnson et al., 2002), downloadable from <https://floats.pmel.noaa.gov/gregory-c-johnson-home-page>, referred to as Johnson climatology hereafter. Meridional sections of contemporaneous conductivity-temperature-depth (CTD) and acoustic Doppler current profiler (ADCP) data across the Pacific have been used to construct the climatology of the upper 400 m zonal current in the Equatorial Pacific. The Johnson climatology was constructed primarily during the 1990s and contain ten meridional sections, 143°E, 156°E, 165°E, 180°E, 170°W, 155°W, 140°W, 125°W, 110°W and 95°W. Missing values exist at certain depths and latitudes, particularly the most western section (143°E). Johnson data are unusual in that they allow direct estimates of properties of the near-equatorial currents, especially including the measurement of tropical upper ocean current velocity. The use of direct velocity data can allow inclusion of ageostrophic effects both around the equator and away from it. For example, the subsurface velocity maximum in the NECC is the combination of the wind-driven Ekman layer and geostrophic shear, a feature that geostrophic calculations alone would not resolve. This dataset thus adds additional information to the longer record from MIMOC which is based on geostrophy alone.

The salinity and temperature data from MIMOC (Monthly Isopycnal and Mixed-layer Ocean Climatology, Schmidtko et al., 2013, downloadable from <https://www.pmel.noaa.gov/mimoc/>) also have been used to evaluate the model results. The monthly climatological MIMOC data have been used to calculate the geostrophic currents in the upper 400 m. In addition, the ocean current from the SODA 2.2.4 reanalysis (Giese and Ray, 2011), downloadable from [http://apdrc.soest.hawaii.edu/datadoc/soda\\_2.2.4.php](http://apdrc.soest.hawaii.edu/datadoc/soda_2.2.4.php) is used to compute the volume transport.

## 2.2. Numerical experiments

The Community Earth System Model version 2 (CESM2) has been employed here. A displaced North Pole grid with a nominal 1° horizontal resolution (meridional resolution increased to 0.27° near the equator) is used in its ocean component (Parallel Ocean Program 2, POP2). POP2 has 60 vertical levels, monotonically increasing from 10 m (upper 150 m) to 250 m in the deep ocean (Danabasoglu et al., 2014). The atmospheric component of CESM2 is the version 6.0 of the Community Atmosphere Model (CAM6), with a finite volume nominal resolution of 1° ( $0.9^\circ \times 1.25^\circ$ ) and 30 vertical levels. The Community

Ice CodE version 5 (CICE5) and the Community Land Model version 5 (CLM5) are used.

In order to analyze the impacts of new forcing datasets and feedback of surface ocean current on the tropical ocean currents simulation, two sets of experiments are designed in our research. The first set contains four experiments (Table 1): (i) a standard ocean-sea ice experiment (POP2 coupled to CICE5), forced by the uncorrected JRA-55 forcing dataset. The surface ocean current is included when calculating the surface wind stress ( $\vec{\tau}$ ), referred to as the “JRA-Raw-OC” experiment hereinafter. (ii) Similar to the experiment (i), but the surface ocean current is not included when calculating the surface wind stress, referred to as the “JRA-Raw-NC” experiment. (iii) A standard ocean-sea ice experiment, forced by the corrected JRA-55 forcing dataset, version 1.1. The surface ocean current is included when calculating the surface wind stress, referred to as the “JRA-Do-OC” experiment hereinafter. (iv) Similar to the experiment (iii), but the surface ocean current is not included when calculating the surface wind stress, referred to as the “JRA-Do-NC” experiment. These four POP2 experiments are all initialized with the January climatology in the World Ocean Atlas 2013 version 2 and run for two cycles (1958 to 2009). As mentioned above, there are obvious differences in the wind correction between the first two and the third phase (Figure 10 and Figure 11 in Tsujino et al., 2018). Here, the attention is paid to the phase-III wind correction only (1998–present), during which the QuikSCAT data has been employed to correct the surface wind. The results from the period of 1998–2007 are used for the analysis. We notice that the difference between corrected JRA-55 (JRA55-do) and uncorrected JRA-55 is not just in wind, but in all other variables, such as temperature, humidity, etc. According to Sun et al. (2019), the changes to wind forcing will be more important to NECC than changes to other variables.

The second set of numerical experiments attempts to investigate the effect of double-counting ocean currents on the NECC simulation using both the fully coupled model and the ocean only model, CESM2 and POP2, respectively. Three experiments have been conducted (Table 2): (i) a 140-year preindustrial control run of CESM2 (hereafter referred to as the “CESM”) based on the 1850 greenhouse gas emissions. The surface atmospheric variables from this experiment are saved hourly as forcing data for the additional two experiments: (ii) a 10-year ocean-sea ice coupled experiment forced by the last 10-years (year-131 to 140) hourly atmospheric output of the coupled CESM (hereafter referred to as the “POP-F”), starting from the end of 130th year; (iii) same as (ii) POP-F but in which the last 10-year mean ocean surface currents are subtracted from the lowest level atmospheric winds (50 m, the top of the surface layer of the planetary boundary layer) before computing the surface wind stresses, to mimic the double-counting process of the ocean current feedback in JRA55-do data. This experiment is called POP-FS hereafter. The last 10 years of these three experiments (CESM/POP-F/POP-FS) are analyzed. It should be noted that, ideally, to be consistent with consideration of QuikSCAT 10 m winds, the mean surface currents should be subtracted from coupled model 10 m winds, rather than the 50 m winds in the POP-FS experiment. However, the software infrastructure in CESM made this option impractical.

## 2.3. Diagnostic analysis offline

The NECC transport can be estimated using the surface wind stress based on Sverdrup's linear theory. Therefore, we also estimated the impact of surface currents feedback using this offline alternative. Using the same bulk formula within the CESM (Large and Yeager, 2009), we can calculate the wind stress with and without the effects of surface ocean current, and then estimate the corresponding Sverdrup transports. The atmospheric states are from the 3-hourly atmospheric JRA55-raw data. The ocean surface currents and the sea surface temperature are from 5-day Ocean Surface Current Analyses Real-time (OSCAR) data (Johnson et al., 2007); downloadable from [https://podaac-opendap.jpl.nasa.gov/opendap/allData/oscar/L4/oscar\\_1\\_deg/](https://podaac-opendap.jpl.nasa.gov/opendap/allData/oscar/L4/oscar_1_deg/)

**Table 1**

The configurations for the first group experiments.

Num	Exp.	Model	Forcing data	Ocean current	Integral time	Period for analysis
1	JRA-Raw-OC	POP2	JRA-raw	Yes	2 cycles	1998–2007
2	JRA-Raw-NC	POP2	JRA-raw	No	2 cycles	1998–2007
3	JRA-Do-OC	POP2	JRA55-do-v1.1	Yes	2 cycles	1998–2007
4	JRA-Do-NC	POP2	JRA55-do-v1.1	No	2 cycles	1998–2007

**Table 2**

The configurations for the second group experiments.

Num	Exp.	Model	Forcing data	Integration time	Period for analysis
1	CESM	CESM2	–	140 years	130–140
2	POP-F	POP2	The output data from Exp. CESM with absolute wind	10 years	1–10
3	POP-FS	POP2	The output data from Exp. CESM with relative wind	10 years	1–10

and daily Optimum Interpolation Sea Surface Temperature (OISST) v2.0 data (Reynolds et al., 2007), downloadable from <https://www.ncdc.noaa.gov/oisst>.

Four experiments are designed here. (i) The surface ocean current is not included in the bulk formula when the wind stress is calculated, referred to as the “Uo\_No” experiment. (ii) The surface ocean current is included once in the bulk formula, referred to as the “Uo\_Once” experiment. (iii) The surface ocean current is included twice in the bulk formula, referred to as the “Uo\_Twice” experiment. (iv) The main effects of the surface ocean current on the wind stress are quantified with a simplified bulk formula, referred to as the “Uo\_Only” experiment. The formulation details are provided in Section 2.4.

#### 2.4. The effect of the current feedback on the wind stress

The typical bulk formula calculating the surface wind stress (ocean surface current included) is as follows:

$$\vec{\tau} = \rho_a * C_{DN} * |\vec{U}_a - \alpha * \vec{U}_o| * (\vec{U}_a - \alpha * \vec{U}_o) \quad (1)$$

where  $\rho_a$  is the near surface air density;  $\vec{U}_a$  is the 10 m atmospheric wind vector;  $\vec{U}_o$  is the ocean surface currents;  $C_{DN}$  is the drag coefficient, calculated from the 10 m wind vector ( $\vec{U}_a$ ), 10 m specific humidity, 10 m air temperature, sea level pressure and sea surface temperature.  $\alpha$  is the specified parameter controlling the inclusion of ocean surface current with three options, i.e., 0 for the EXP. Uo\_No, 1 for the EXP. Uo\_Once, and 2 for the EXP. Uo\_Twice. Here, the sea level pressure is used to translate the 10 m air temperature to the 10 m potential temperature (Large and Yeager, 2009). The absolute value in Eq. (1) is computed as  $|\vec{U}_a - \alpha * \vec{U}_o| = \sqrt{(u_a - \alpha * u_o)^2 + (v_a - \alpha * v_o)^2}$ .

According to Jullien et al. (2020), the effect of the ocean current feedback on the wind stress (EXP. Uo\_Only) can be explicitly derived from Eq. (1).

$$\vec{\tau}_{U_o\_Only} = \rho_a * C_{DN} * |\vec{U}_a - \vec{U}_o| * (\vec{U}_a - \vec{U}_o) - \rho_a * C_{DN} * |\vec{U}_a| * (\vec{U}_a) \quad (2)$$

Considering  $|\vec{U}_a| \gg |\vec{U}_o|$ , it follows that:

$$|\vec{U}_a - \vec{U}_o| \approx \sqrt{|\vec{U}_a|^2 - 2|\vec{U}_a||\vec{U}_o| \cos\theta} \approx |\vec{U}_a| \sqrt{1 - 2\frac{|\vec{U}_o|}{|\vec{U}_a|} \cos\theta} \quad (3)$$

$\theta$  is the angle between  $\vec{U}_a$  and  $\vec{U}_o$ . With  $\sqrt{1 - x} = 1 - \frac{x}{2}$  if  $|x| \approx 0$ , Eq. (3) becomes:

$$|\vec{U}_a - \vec{U}_o| \approx |\vec{U}_a| \left( 1 - \frac{|\vec{U}_o|}{|\vec{U}_a|} \cos\theta \right) \approx |\vec{U}_a| - |\vec{U}_o| \cos\theta \quad (4)$$

Similarly, Eq. (2) becomes:

$$\begin{aligned} \vec{\tau}_{U_o\_Only} &\approx \rho_a * C_{DN} * \left[ (|\vec{U}_a| - |\vec{U}_o| \cos\theta) (\vec{U}_a - \vec{U}_o) - |\vec{U}_a| \vec{U}_a \right] \\ &\approx -\rho_a * C_{DN} * \left( |\vec{U}_a| \vec{U}_o + \vec{U}_a |\vec{U}_o| \cos\theta \right) \end{aligned} \quad (5)$$

#### 2.5. Zonal transport of NECC

To understand the dynamics of NECC in these experiments, the annual mean vorticity balance is calculated following Kessler et al. (2003) and Sun et al. (2019). The equation for the zonal transport is derived from momentum equations as follows:

$$U = \frac{1}{\beta} \int_x^{EB} \text{curl}(\tau^*)_y dx + U_{EB} \quad (6)$$

Here,  $\tau^* = \vec{\tau} - \vec{A} + \vec{F} - \nabla \vec{P} - \frac{\partial \vec{V}}{\partial t}$ , which represents surface wind stress ( $\vec{\tau}$ ), advection ( $-\vec{A}$ ), friction ( $\vec{F}$ ), horizontal pressure gradient ( $-\nabla \vec{P}$ ) and the tendency of the horizontal ocean current terms ( $-\frac{\partial \vec{V}}{\partial t}$ ), respectively (Kessler et al., 2003). Among them,  $\vec{A} = (A^x, A^y) = \int \nabla \cdot (\vec{u} \vec{h} \vec{u}) ds$ , represents the vertically integrated horizontal momentum flux.  $\vec{F} = (F^x, F^y)$ , represents the boundary friction.  $U_{EB}$  is the transport at the eastern boundary (EB). The stream function form of Eq. (6) is used to compute  $U$  to avoid the uncertainties of the value of  $U_{EB}$  as (Kessler et al., 2003):

$$U = -\varphi, \quad (7)$$

$\varphi = \frac{1}{\beta} \int_{x(y)}^X \text{curl}(\tau^*)_y dx$  is the stream function of vertically integrated volume transport. The values of  $\varphi$  along the coast of the Americas are assigned to 0. As in Sun et al. (2019), we integrate the total transport from the surface to 400 m, comparable with 353 m used in Kessler et al. (2003). Qualitatively similar results can be obtained when we integrate the upper 200 m. This equation is also used to estimate the zonal transport of NECC offline, in which only the surface wind stresses are used to compute  $\tau^*$ .

## 3. Results

### 3.1. The NECC simulation in ocean–sea ice coupled model forced by new JRA55-do dataset

To investigate the NECC simulation in ocean–sea ice coupled model forced by new JRA55 dataset, the zonal currents vertically integrated over the upper 400 m are compared in Fig. 2a–d from four experiments, JRA-Raw-OC, JRA-Raw-NC, JRA-Do-OC and JRA-Do-NC. The eastward Pacific NECC between 3° and 10°N is accompanied by the westward North (South) Equatorial Current (NEC/SEC) at its northern (southern) flank, and the eastward Equatorial Undercurrent (EUC) is located at the equator beneath the surface current. The comparison indicates that both surface wind correction and considering ocean current in the bulk formula significantly weaken the Pacific NECC, especially west of 120°W. Both JRA-Do experiments exhibit a bias of weak NECC similar to the CORE simulations by Sun et al. (2019).

The volume transport of the NECC, defined as the meridional integration of upper 400-m eastward transports between 3° and 10°N, is further estimated (solid lines) and compared with Johnson climatology (black dots, Fig. 2e). Both the QuikSCAT correction and whether or

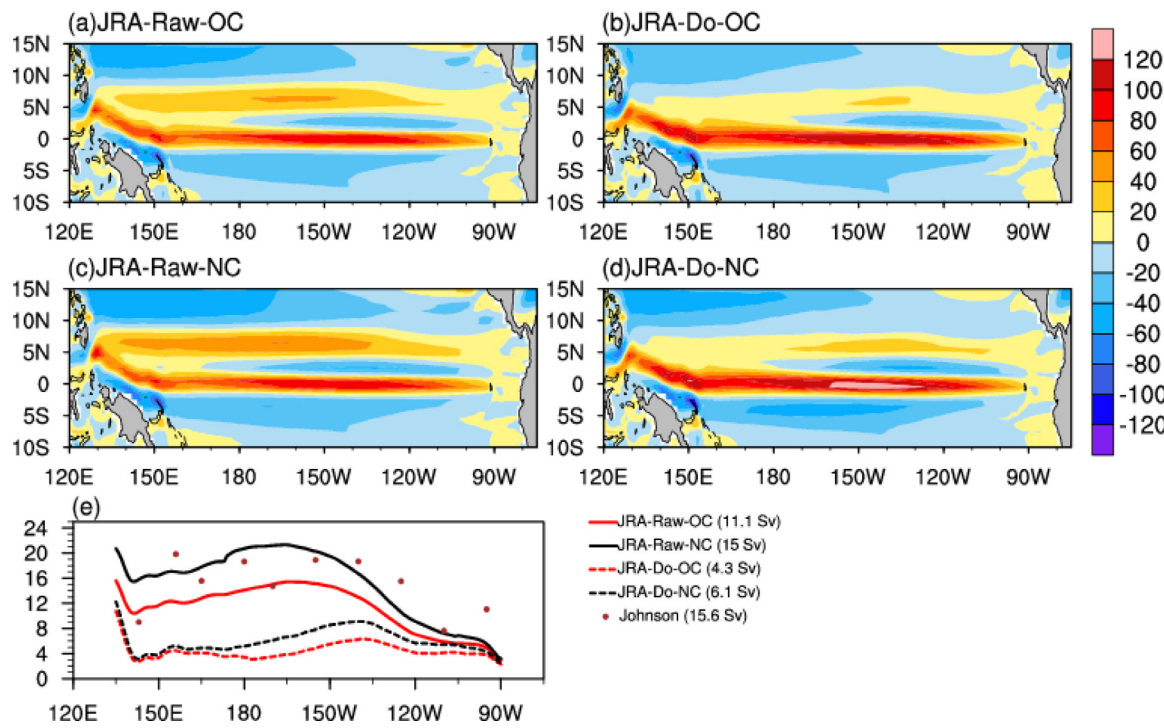


**Fig. 2.** The upper 400 m vertically integrated zonal currents (Units:  $\text{m}^2 \text{ s}^{-1}$ ) for experiment (a) JRA-Raw-OC, (b) JRA-Do-OC, (c) JRA-Raw-NC and (d) JRA-Do-NC. The NECC volume transports (unit: Sv), which are defined as the meridionally integrated upper 400 m eastward transport between  $3^\circ\text{N}$ - $10^\circ\text{N}$ , (e) for experiment JRA-Raw-OC (red solid line), JRA-Raw-NC (black solid line), JRA-Do-OC (red dash line), JRA-Do-NC (black dash line) and Johnson et al. (2002) observation (black dots). Inside the brackets is the average NECC transports between  $150^\circ\text{E}$  and  $90^\circ\text{W}$ . The average time is 1998–2007.

**Table 3**

The total NECC transports and the Sverdrup transports of NECC for Johnson observation and four JRA experiments (Unit: Sv) (average between  $150^\circ\text{E}$  and  $90^\circ\text{W}$ ).

	Johnson	JRA-Raw-OC	JRA-Raw-NC	JRA-Do-OC	JRA-Do-NC
The total NECC transport	15.6	11.1	15.0	4.3	6.1
The Sverdrup transports of NECC	–	15.2	21.7	7.7	11.9

not the ocean currents are taken into account in the bulk formula significantly affect the simulation of NECC. The average zonal volume transports of NECC for each experiment are shown in Table 3. The QuikSCAT correction leads to the NECC transports weakened by 61% (from 11.1 Sv in the JRA-Raw-OC to 4.3 Sv in the JRA-Do-OC) and 60% (from 15.0 Sv in the JRA-Raw-NC to 6.1 Sv in the JRA-Do-NC), respectively. The inclusion of the ocean current in the bulk formula weakens the average NECC transports by 26% (from 15.0 to 11.1 Sv) for the raw data (JRA-Raw-NC and JRA-Raw-OC) and 30% (from 6.1 to 4.3 Sv) for corrected data (JRA-Do-NC and JRA-Do-OC). Overall, the effect of QuikSCAT correction mainly comes from the differences between QuikSCAT winds and the JRA-raw reanalysis winds, and the effect of ocean current is also part of it.

The impacts of these two procedures are most evident west of  $120^\circ\text{W}$ . We note that the zonal transport of Pacific NECC in the JRA-Raw-NC is closest to the observations. However, the bulk formula in the JRA-Raw-NC experiment is not consistent with the actual process of momentum transfer at the air-sea interface because the ocean current should be considered in the wind stress calculation (Kelly et al., 2001; Cornillon and Park, 2002; Large and Yeager, 2004; Hersbach and Bidlot, 2008). By including the effect of the ocean currents in air-sea momentum transfer, the zonal transport of Pacific NECC is about 30% weaker in the JRA-Raw-OC than Johnson's observation, suggesting other factors in the JRA-raw reanalysis winds, in addition to the QuikSCAT correction, may also contribute to the weak Pacific NECC in POP2 simulation. In the present study we focus mainly on the impacts of forcing wind dataset corrected with QuikSCAT.

To further confirm these impacts, the geostrophic currents estimated from the MIMOC data are compared with model results at three meridional–vertical sections ( $180^\circ\text{E}$ ,  $140^\circ\text{W}$  and  $110^\circ\text{W}$ ; Fig. 3). Here, the climatological zonal current of Johnson climatology is also shown for comparison (leftmost panel in Fig. 3). All modeled strengths of Pacific NECC over the whole Pacific are much weaker than those estimated from MIMOC. The maximum velocity of Pacific NECC for MIMOC is about  $0.2 \text{ m s}^{-1}$ ,  $0.3 \text{ m s}^{-1}$  and  $0.15 \text{ m s}^{-1}$  at  $180^\circ\text{E}$ ,  $140^\circ\text{W}$ , and  $110^\circ\text{W}$ , respectively compared to modeled maximum velocities around  $0.1 \text{ m s}^{-1}$  at these three sections. The same conclusion holds for different time spans for temporal averaging, indicating the robustness of the above-mentioned results.

Fig. 4 shows the WSCs and corresponding zonal Sverdrup transports (ZST) in the four experiments based on JRA forcing. Note the ZST can be viewed as the direct impact of the surface wind stresses on the NECC. The eastward (positive) ZSTs between  $3^\circ\text{N}$  and  $10^\circ\text{N}$  are related to the NECC while the eastward ZSTs along the equator are due to the EUC. We note that the weak EUC in the JRA55-Raw-\* numerical experiments are partly due to the bias of JRA55-raw reanalysis dataset, which has been improved in the JRA55-do wind dataset and hence a stronger EUC is obtained in the JRA55-Do-\* numerical experiments. The ZSTs from NECC averaged over  $150^\circ\text{E}$  and  $90^\circ\text{W}$  for each experiment are shown in Table 3. The QuikSCAT wind correction weakened the NECC-induced ZST 49% for OC experiments and 45% for NC experiments. Meanwhile, the NECC-induced ZST is also reduced by about 30% if the ocean current is taken into account in the bulk formula (30% for JRA-Raw-OC/JRA-Raw-NC and 35% for JRA-Do-OC/JRA-Do-NC). These results

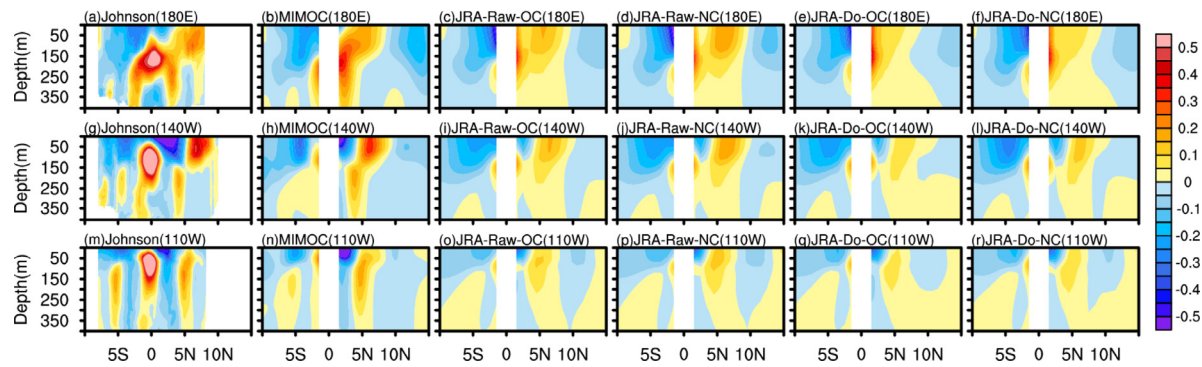


**Fig. 3.** Meridional-vertical sections of annual mean zonal currents (Units:  $\text{m s}^{-1}$ ) at (a)  $180^\circ\text{E}$ , (g)  $140^\circ\text{W}$ , and (m)  $110^\circ\text{W}$  for climatological Johnson observation data; (b)/(h)/(n) is the geostrophic zonal currents for climatological MIMOC data. (c)/(i)/(o) is the geostrophic zonal currents for experiment JRA-Raw-OC. (d)/(j)/(p) is the geostrophic zonal currents for experiment JRA-Raw-NC. (e)/(k)/(q) is the geostrophic zonal currents for experiment JRA-Do-OC. (f)/(l)/(r) is the geostrophic zonal currents for experiment JRA-Do-NC (Unit:  $\text{m s}^{-1}$ ). The average time for model results is 1998–2007. The values between  $1^\circ\text{S}$  and  $1^\circ\text{N}$  are set to the default for geostrophic zonal currents.

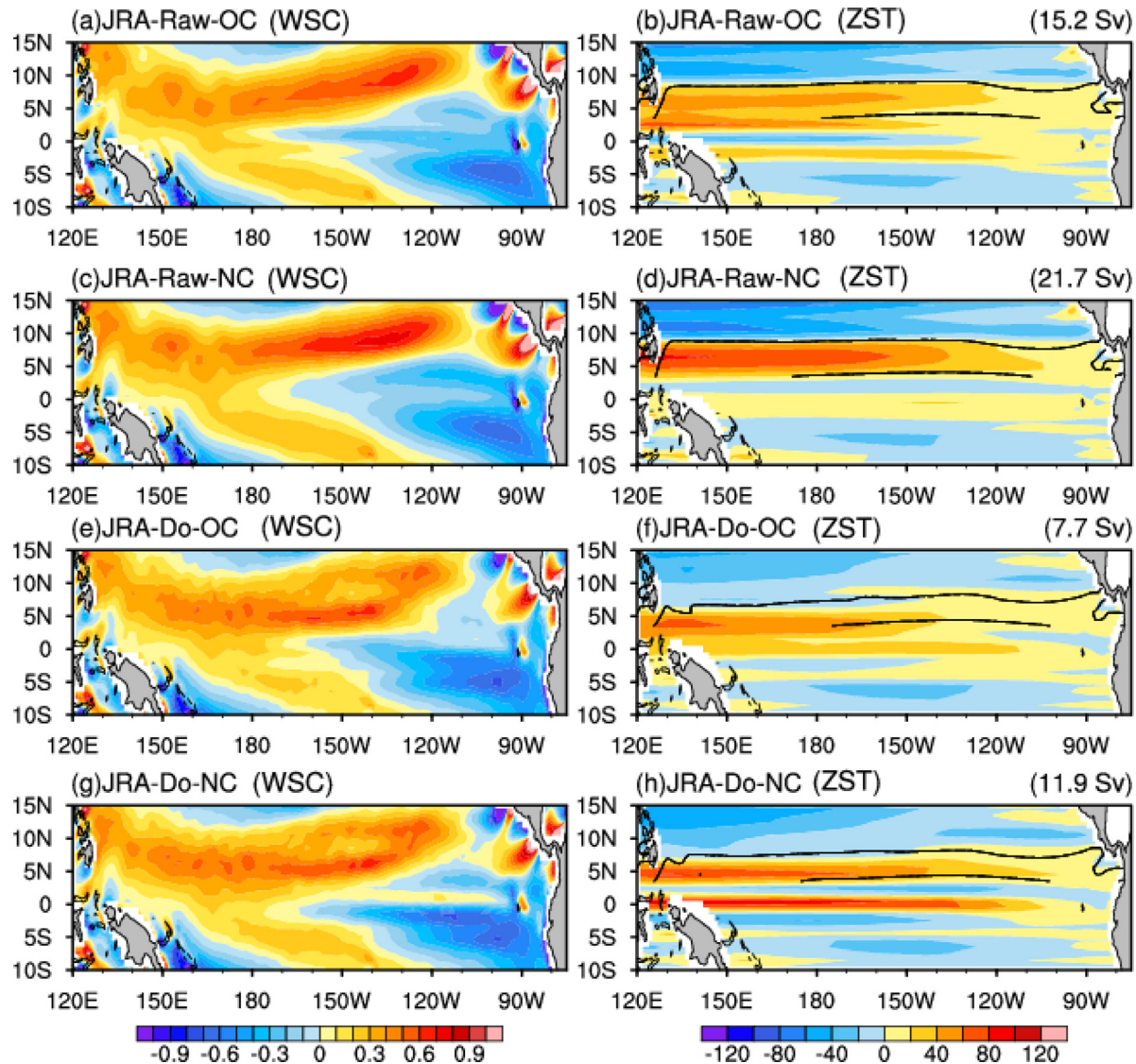


**Fig. 4.** The average wind stress curl (WSC, Unit:  $\text{N m}^{-3} \times 10^{-7}$ ) contributed by the wind stress calculated from experiment (a) JRA-Raw-OC, (c) JRA-Raw-NC, (e) JRA-Do-OC, (g) JRA-Do-NC. The zonal Sverdrup transports (ZST, Unit:  $\text{m}^2 \text{s}^{-1}$ ) contributed by the wind stress calculated from experiment (b) JRA-Raw-OC, (d) JRA-Raw-NC, (f) JRA-Do-OC, (h) JRA-Do-NC. The contours in the figure (b)/(d)/(f)/(h) are the zero-line of the eastward 400 m depth-integrated ocean current between  $3^\circ\text{N}$  and  $10^\circ\text{N}$  for the total transport which is shown in Fig. 2a (for JRA-Raw-OC), Fig. 2b (for JRA-Raw-NC), Fig. 2c (for JRA-Do-OC) and Fig. 2d (for JRA-Do-NC), respectively. The values in the upper right corner of figure are the average NECC zonal Sverdrup transports contributed by the wind between  $150^\circ\text{E}$  and  $90^\circ\text{W}$ . The average time is 1998–2007.

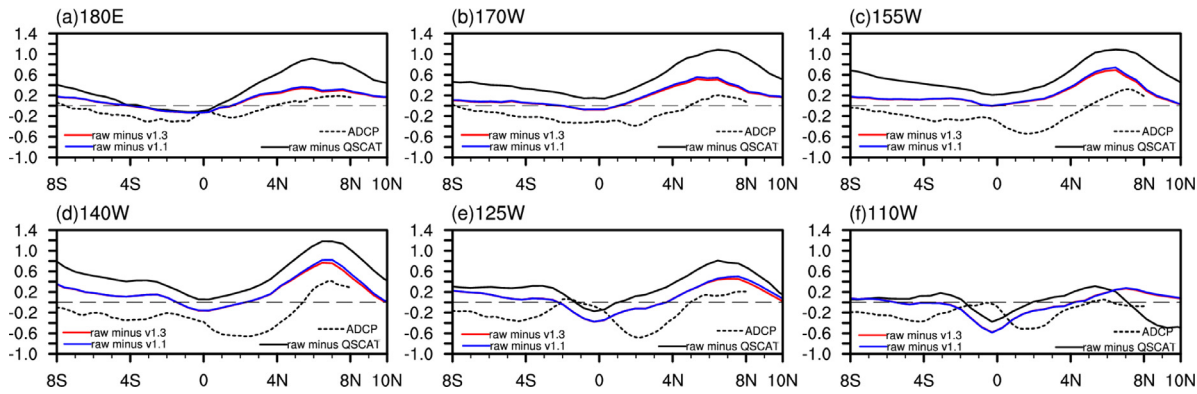


**Fig. 5.** The difference of 10 m zonal wind between JRA-raw and JRA55-do-v1.3 (JRA-raw minus JRA55-do-v1.3; red solid line; units:  $\text{m s}^{-1}$ ), JRA-raw and JRA55-do-v1.1 (JRA-raw minus JRA55-do-v1.1; blue solid line; units:  $\text{m s}^{-1}$ ), JRA-raw and QuikSCAT (JRA-raw minus QuikSCAT; black solid line; units:  $\text{m s}^{-1}$ ). The observed surface ocean current (black dash line; units:  $\text{m s}^{-1}$ ; Johnson et al., 2002) for the longitude of (a) 180°E, (b) 170°W, (c) 155°W, (d) 140°W, (e) 125°W and (f) 110°W. The average time for JRA-55 wind data is 1998–2009, for ocean current data of Johnson et al. is 1986–2000.

are generally consistent with the reduction of total ZST of NECC shown in Fig. 2, but the actual contribution differs due to other nonlinear forcing terms, for example, the advection and friction terms, rather than the wind itself (Sun et al., 2019).

Two patches of maximum WSC can be found in the adjusted data on both sides of 7°N for JRA-Do-OC and JRA-Do-NC between 170°W and 130°W, showing a zonal belt of positive WSC splitting into two parts in the ITCZ region. However, only one maximum center exists in the JRA-Raw-OC and JRA-Raw-NC datasets. These WSC differences result from the wind correction procedure using the scatterometer equivalent neutral winds (i.e., QuikSCAT) and have been identified in the CORE data (Figure 6a in Sun et al., 2019). The split branches of positive WSC in the ITCZ region are also clear in the climatological QuikSCAT results (Figure 58, Tsujino et al., 2018), possibly resulting from the retrieval biases in QuikSCAT wind data (Milliff et al., 2004; Kilpatrick and Xie, 2016). The cause and effect of this split require further investigation but are beyond the scope of this study. It has been verified that the signature of surface ocean current is contained in the QuikSCAT wind data (Figure 3 in Kelly et al., 2001). Is there any surface current signal in the corrected forcing datasets? Fig. 5 compares the 10 m zonal wind differences between different products with the data of Johnson et al. (2002) at six meridional sections (180°E, 170°W, 155°W, 140°W, 125°W, 110°W). For the observed surface ocean current data of Johnson et al. positive values exist between 3°N and 10°N and negative values south of 3°N (black dashed lines), representing the eastward NECC and the westward SEC, respectively. In all of these meridional sections, a big offset can be found between the black solid line (difference between JRA55-raw and QuikSCAT) and dashed line (observed surface zonal ocean current) near the NECC region (3°N–10°N). This suggests large systematic errors beyond that related to the surface ocean current may exist in the JRA55-raw wind, for example, the easterly wind in the JRA55-raw is generally weak in the tropical Pacific (180°E–140°W). These systematic errors are universal for reanalysis datasets (Belmonte Rivas and Stoffelen, 2019) and cannot be easily separated here. The meridional profile of the zonal wind difference between JRA55-raw and JRA55-do-v1.1 (the blue solid line in Fig. 5) follows well with the meridional profile of the observed surface zonal ocean current (the dashed line), confirming the inclusion of surface ocean current in the corrected JRA-55 data. Comparing with JRA55-do-v1.1, we only found small changes in the procedure of wind speed correction for JRA55-do-v1.3 (Tsujino et al., 2018), also shown with the relatively small 10-m zonal wind difference between JRA55-do-v1.1 and JRA55-do-v1.3 in Fig. 5 (the blue solid line aligning well with the red solid line).

**Table 4**

The Sverdrup transports of NECC estimated offline (Unit: Sv) (average between 150°E and 90°W).

Exp.	$\alpha = 0$	$\alpha = 1$	$\alpha = 2$	Uo_Only
(Sv)	19.8	13.2	6.8	-6.9

### 3.2. Observation-based analysis on the effect of double-counting of ocean currents

The previous section shows that the simulated NECCs are generally weaker in the OC (JRA-Raw-OC and JRA-Do-OC) than the NC (JRA-Raw-NC and JRA-Do-NC) experiments. Note that because of the inclusion of ocean currents in QuikSCAT data, the surface currents are indeed double-counted in the OC experiments forced by the QuikSCAT-corrected wind product. We further evaluate this weakening impact on the NECC from the perspective of linear Sverdrup theory by using the observational data. In the linear analysis three different types of bulk formulas for the wind stresses (Eq. (1)) represent three different cases, i.e., that of no ocean current feedback ( $\alpha = 0$ ), once-counted ocean current feedback ( $\alpha = 1$ ), and double-counted ocean current feedback ( $\alpha = 2$ ). Then the effect of the ocean currents in the wind stress formula on the NECC may be explicitly estimated using Eq. (5).

Fig. 6 shows that the whole band of positive WSC is separated into two zonal bands, branched at 9°N, when the ocean current is taken into account (compare Fig. 6c and e with Fig. 6a). Induced by the corresponding changes in the meridional gradient of the WSC ( $\text{curl}(\tau_y)$ ) the NECC is weakened with its axis being moved southward (Fig. 6d and f). The effects of ocean current feedback on the ZST are analytically quantified in Fig. 6g and h (from Eq. (5)). A belt of negative meridional gradient of WSC ( $\text{curl}(\tau_y)$ ) is shown and that of negative anomaly in the ZST between 3° and 10°N (near the Pacific NECC) may well explain the reduction of the NECC transport.

The zonal Sverdrup transports (ZSTs) of NECC averaged from 150°E to 90°W are 19.8 Sv ( $\alpha = 0$ ), 13.2 Sv ( $\alpha = 1$ ) and 6.8 Sv ( $\alpha = 2$ ), respectively (Table 4). Here, the zonal Sverdrup transports of NECC are defined as the meridional integration of the Sverdrup transports between 3°N and 10°N. Note the relationship of the weakening of NECC-induced zonal Sverdrup transports with the strength of ocean current feedback in the bulk formula ( $\alpha$ ) is nearly linear, i.e., around -6.6 Sv (33%) from  $\alpha = 0$  to  $\alpha = 1$  (13.2 Sv) and -6.4 Sv from  $\alpha = 1$  to  $\alpha = 2$ , respectively. On the other hand, the reduction of NECC-induced ZST due to the surface current feedback estimated by Eqs. (5) and (6) is -6.9 Sv, basically consistent with the above-mentioned estimates, suggesting that it is reasonable to quantify the impact of ocean current

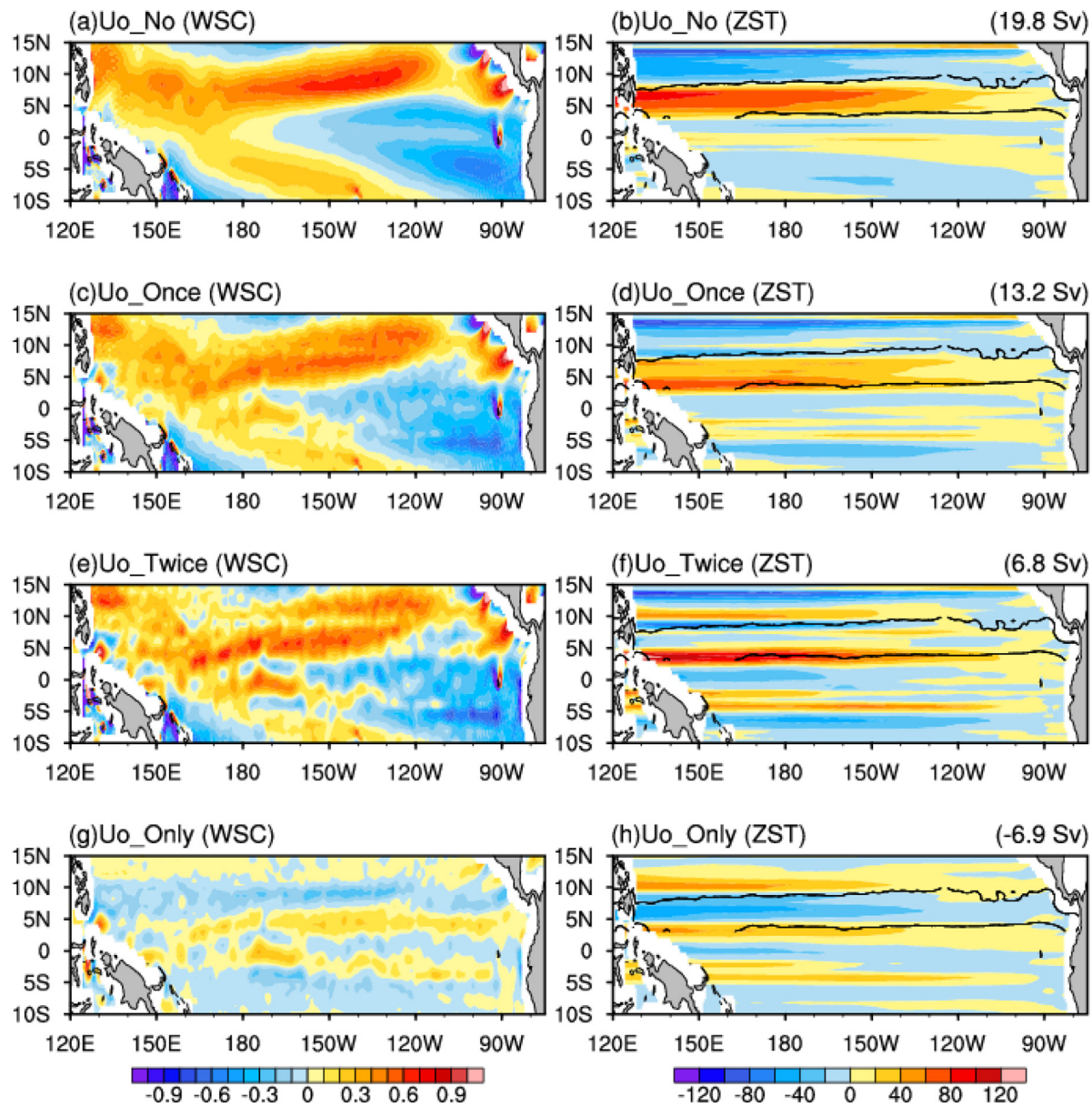


**Fig. 6.** Annual mean wind stress curl (WSC, Unit:  $\text{N} \cdot \text{m}^{-2}$ ) for (a) (EXP, Uo\_No), (c) (EXP, Uo.Once), (e) (EXP, Uo.Twice) and (g) (EXP, Uo.Only). Annual mean zonal Sverdrup transports contributed by the wind (ZST, Unit:  $\text{m}^2 \cdot \text{s}^{-1}$ ) for (b) (EXP, Uo\_No), (d) (EXP, Uo.Once), (f) (EXP, Uo.Twice) and (h) (EXP, Uo.Only). The contours in the figure (b)/(d)/(f)/(h) are the zero-line of the eastward 400 m depth-integration ocean current between  $3^\circ\text{N}$  and  $10^\circ\text{N}$  for the total transport calculated with SODA reanalysis data. The values in the upper right corner of figure are the average ( $150^\circ\text{E}$ - $90^\circ\text{W}$ ) NECC zonal Sverdrup transports. The average time is 1999–2006.

on the NECC simulation using Eq. (5). Comparing this 6.9 Sv reduction with the 6.5 Sv reduction in the experiments forced by JRA-55 data (21.7 Sv in JRA-Raw-NC and 15.2 Sv in JRA-Raw-OC, respectively), we believe the observation-based offline experiments are generally consistent with above two JRA-Raw numerical experiments.

### 3.3. The effects of double-counted surface ocean currents on the NECC simulation in a “perfect” experiment

We further quantify the impacts of double-counted surface ocean currents (within the bulk-formula) on the resulting NECC simulation using a set of “perfect” CESM2 sensitivity experiments. Here “perfect” is meant by the internal consistency between the experiments and the exclusion of possible inconsistencies between the different data sources, observational and/or of reanalysis. First a coupled simulation with the CESM2 under the preindustrial climate forcing is performed (see Section 2.1 for details). Then POP-F, a standard OMIP-type experiment

forced by the last 10-year atmospheric state of the coupled CESM2 simulation, is performed. Similarly, we further performed the POP-FS experiment, in which we subtract the last 10-year-averaged surface currents of coupled CESM2 simulation from the lowest level winds of the CESM2 simulation before calculating the surface wind stresses, which mimics the double-counting process of the ocean current feedback in the JRA55-do data. Fig. 7a and b compare the meridional profiles of the mean zonal current at  $180^\circ\text{E}$  for POP-F and POP-FS experiments, respectively. The results from the coupled CESM2 simulation are not shown here, since they are indistinguishable from the results from the POP-F experiment. The mean speed of NECC in the POP-FS is approximately  $0.2 \text{ m s}^{-1}$ , about  $0.1 \text{ m s}^{-1}$  weaker than that in the POP-F ( $0.3 \text{ m s}^{-1}$ ) experiment. Similarly, the SEC and NEC speeds are also reduced by around  $0.1 \text{ m s}^{-1}$  in the POP-FS experiment, while the EUC is almost unaffected.

Fig. 7c and d show the zonal NECC transports in POP-F and POP-FS, respectively. This depth-integrated modeled zonal transport can be

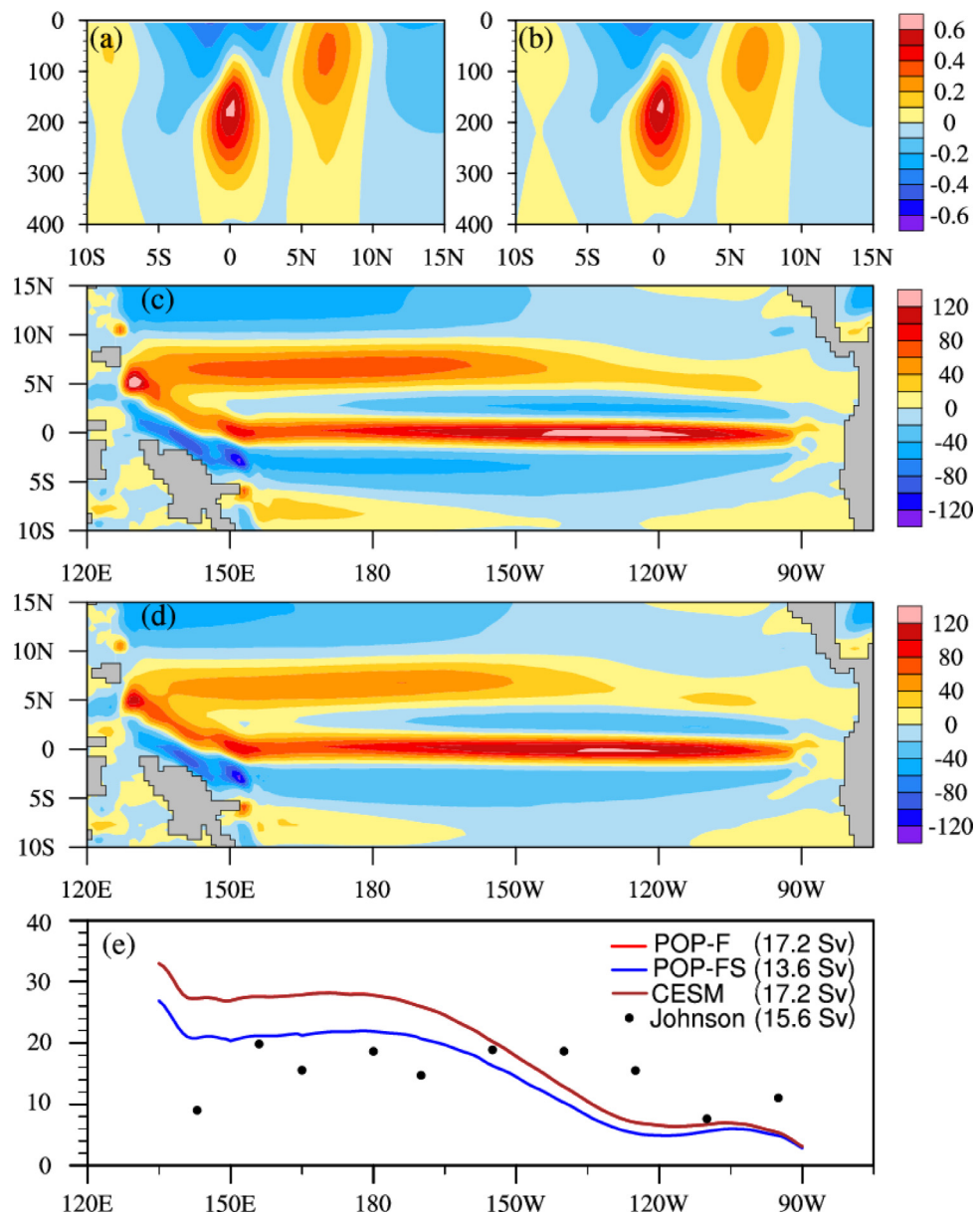


**Fig. 7.** Meridional-vertical sections of annual mean zonal currents at 180°E for (a) POP-F and (b) POP-FS (Unit:  $\text{m s}^{-1}$ ). The upper 400 m vertically integrated zonal currents (Units:  $\text{m}^2 \text{s}^{-1}$ ) for (c) POP-F and (d) POP-FS (Units:  $\text{m}^2 \text{s}^{-1}$ ). (e) is the volume transports of NECC (Unit: Sv), which are defined as the meridionally integrated eastward transport between 3°N and 10°N, for CESM (brown solid), POP-F (red solid), POP-FS (blue solid) and Johnson climatology (black dots). Inside the brackets are the average NECC transports between 150°E and 90°W. Please notice that the curves for CESM and POP-F are overlapped.

directly compared with the Sverdrup transport. Both experiments have the maximum NECC transports west of 150°W while the maximum NECC transport (over  $60 \text{ m}^2 \text{s}^{-1}$ ) in the POP-F is larger than that in the POP-FS. Fig. 7e compares the total transports of NECC (solid lines). The NECC transports in the CESM2 simulation and in the POP-F experiment are nearly identical, as expected due to the almost identical atmospheric forcing used in the two experiments. It is apparent that the NECC transport in the POP-F (~17.2 Sv) experiment is generally greater than that in the POP-FS (13.6 Sv) within 150°E–90°W. This suggests the NECC is weakened by about 3.6Sv (around 21%) if the surface ocean currents are calculated twice within the bulk formulation.

The above-mentioned linear Sverdrup analysis suggests the ocean current impacts are about  $-6.6$  or  $-6.4$  Sv (Table 4), much stronger than  $-3.6$  Sv, the difference between POP-F and POP-FS experiments. The bigger ocean current impacts in linear Sverdrup analysis may come from the inconsistencies between the different data sources used, observational and/or of reanalysis. It is also possible that the built-in

nonlinear processes within the model partly damp the reduction of the NECC transport due to the double counting.

We further compare the mean zonal wind stress (ZWS), WSC and the corresponding ZST in the POP-FS and POP-F experiments (Fig. 8), respectively, with their differences (POP-FS minus POP-F) being presented at the bottom panel of Fig. 8. In the POP-FS experiment, the double-counted surface ocean currents lead to a negative ZWS difference over 3°N–10°N, just above NECC, and positive differences above the SEC (6°S–3°N) and NEC (10°–15°N) regions (Fig. 8g). While the magnitudes of these ZWS anomalies are relatively small (less than 10%) compared with the wind stress itself, but they may significantly affect the WSC via the meridional gradient of ZWS. The changes of the zonal wind pattern, reducing over the NECC and increasing over the SEC and NEC, result in positive WSC over 3°–6°N and negative WSC over 6°–14°N (Fig. 8h), and hence result in a belt of negative zonal Sverdrup transport (ZST) anomaly over the NECC latitudes since the meridional gradient of the WSC,  $\text{curl}(\tau)_y$ , is the dominant term

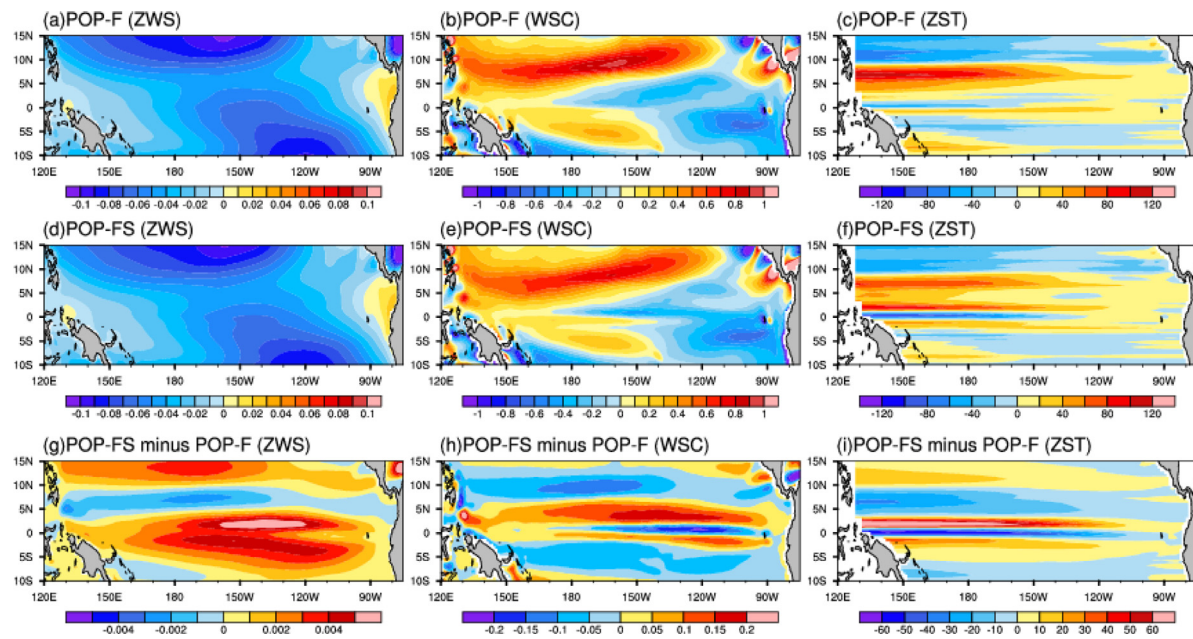


Fig. 8. Annual mean zonal wind stress (ZWS) for (a) POP-F, (d) POP-FS and (g) the difference between POP-FS and POP-F (Unit:  $N\ m^{-2}$ ). (b) (e) (h) and (c) (f) (i) are the same as (a) (d) (g), but for the mean wind stress curl (WSC, Unit:  $N\ m^{-3}$ ) and the zonal Sverdrup transport (ZST, Unit: Sv), respectively.

for the ZST. The NECC transports averaged between  $150^{\circ}\text{E}$  and  $90^{\circ}\text{W}$  attributed by the wind differences are 20.1 Sv and 14.2 Sv for POP-F and POP-FS experiments, and hence the double-counting of the ocean surface current reduces the volume transport of NECC by about 5.9 Sv. It should be noted that other processes, such as the advection and diffusion processes, tend to compensate the reduction caused by the wind stresses (figures not shown), and that these impacts are limited to the tropical region only. No significant impacts are identified outside the tropical region, even over the western boundary currents (WBCs) and Antarctic Circumpolar Current (ACC, Figure S1), where the surface currents are as strong as those in the tropical Pacific.

#### 4. Summary and discussion

In the present study, we find that the weak NECC identified in ocean model runs forced by CORE-II dataset for OMIP-1 still occurs when the new JRA55-do dataset (Japanese 55-year Reanalysis adjusted for driving ocean models) for OMIP2 forcing data is used. The simulated zonal transport is about 11.3 Sv (72%) weaker than the Johnson observation (4.3 Sv in JRA-Do-OC compared with 15.6 Sv in the Johnson observation). The QuikSCAT correction procedure and whether or not the modeled ocean current is considered in the bulk formula can significantly affect the Pacific NECC. The QuikSCAT correction weakens the averaged NECC transports by about 60%. Taking the ocean currents into account in the bulk formula may weaken the averaged NECC transports by about 26%–30%. The above two procedures are used together to force the ocean models in the Ocean Model Intercomparison Program (OMIP) currently, and it will cause the bias of double-counting current feedback when calculating the momentum budget (wind stress) in the bulk formula, since the QuikSCAT estimates the equivalent 10-m neutral winds relative to the motion of the ocean surface.

Next, we systematically verify and investigate the impacts of double-counting the ocean surface currents on the modeled Pacific NECC using the typical surface wind stress bulk calculation and linear Sverdrup transport analysis. Using observational data of wind and surface current confirms that including the ocean current in the bulk formula may reduce ZST by around 6.6 Sv (33%) and the further double-counting of the ocean current leads to an additional reduction of 6.4 Sv (48%). Using the CESM2 numerical experiments, we identify that the double-counting in the bulk formula results in approximately 21% weakened

volume transport. The built-in nonlinear processes in the model may partly damp the reduction due to the double-counting of the ocean current.

It seems that the double-counting effects of the current feedback is only evident in the equatorial Pacific and no significant impacts are identified outside the tropical region in our coarse resolution model experiments ( $\sim 1^{\circ}$ ), even over the western boundary currents (WBCs) and Antarctic Circumpolar Current (ACC, Figure S1), where the surface currents are as strong as those in the tropical Pacific. Although the QuikSCAT correction weakens the averaged NECC transports significantly, the bias correction of JRA55-raw reanalysis winds using scatterometer dataset is also required to improve the global simulation. Tsujino et al. (2018) has compared the equivalent neutral 10-m wind speeds zonally averaged over the ocean of JRA55-raw and QuikSCAT datasets in their figure 12 and found there is a big difference between them, reaching around 0.5 m/s at  $50^{\circ}\text{S}$ .

Renault et al. (2020) have recently analyzed the recipes for how to force oceanic model dynamics with different existing datasets (both the reanalysis and scatterometer equivalent neutral winds) on the large-scale circulation and mesoscale eddies between  $45^{\circ}\text{S}$  and  $45^{\circ}\text{N}$  with a series of numerical experiments. They do not conduct exactly the same experiments as the present study, and their focus was on ocean eddy energetics, not countercurrents. Having said that, their experiments to mimic forcing ocean model using scatterometer equivalent neutral winds, experiments " $Sc_{CFB}W_{ABS}$ " and " $Sc_{CFB}W_{REL}$ ", can be partially compared with our experiments "JRA-Do-NC" and "JRA-Do-OC", respectively, and the experiments " $R_{NOCFB}W_{ABS}$ " and " $R_{NOCFB}W_{REL}$ " are comparable with our experiments "JRA-Raw-NC" and "JRA-Raw-OC", respectively. The CFB effects were both double-counted in experiment " $Sc_{CFB}W_{REL}$ " and JRA-Do-OC. They found that the double-counting of the surface current will also lead to the reduction of the area-averaged large-scale circulation, but only by about 5%–10%. The reduction of NECC in the present study was around one third (26%–30%). It possibly can be explained by what they measure is a mean value of a larger meridional extent, between  $45^{\circ}\text{S}$  and  $45^{\circ}\text{N}$ , not only just in the NECC region. In addition, the experiments of POP-F and POP-FS are also comparable with experiments " $R_{CFB}W_{REL}$ " and " $Sc_{CFB}W_{REL}$ " in Renault et al. (2020), respectively.

One alternative to approximate the absolute winds and solve the double-counting bias in NECC simulation was proposed in Tsujino

et al. (2018) and Renault et al. (2020), who added the surface current climatology to the corrected JRA-55 winds (JRA55-do). This addition method is similar to Renault et al.'s (2020) experiment “ $R_{CFB} W_{REL}$ ” and the global large-scale ocean circulation is reasonably simulated (Figure 11 of Renault et al., 2020). Experiment “ $R_{CFB} W_{REL}$ ” means forcing the ocean model with Reanalysis-like produced data with the CFB and considering the surface current in the bulk formula without current feedback parameterization. However, the improvement of Pacific NECC simulation with this method may be limited because the double-counting bias can only explain 26%–30% of the Pacific NECC simulation bias and the other part of this bias, around 30%, caused by the correction with QuikSCAT has not been explained. We notice this part of QuikSCAT-corrected NECC simulation bias may be explained by the retrieval biases in QuikSCAT wind data and the use of annual mean climatological wind adjustment factors (Weissman et al., 2002; Milliff et al., 2004; Risien and Chelton, 2008; O'Neill et al., 2015; Chen and Fu, 2017; King et al., 2017; Kilpatrick and Xie, 2016; Xu and Stoffelen, 2020). One possible alternative is to replace QuikSCAT with Advanced Scatterometer (ASCAT) dataset when correcting the JRA55-raw wind field (Stoffelen et al., 2019; Wang et al., 2019). Bentamy et al. (2012) compared ASCAT and QuikSCAT surface winds during the overlap period and found a positive zonal strip of the difference between collocated QuikSCAT and ASCAT wind speed (QuikSCAT minus ASCAT), located at tropical Pacific particularly (Figure 3a in Bentamy et al., 2012). Their results suggested that the QuikSCAT-derived wind speed is greater than the ASCAT, which may form an artificial negative/positive WSC on the north/south side of this zonal strip and lead to the negative meridional gradient of WSC and weak Pacific NECC simulation in our comparison. Using ASCAT for the extra surface current adjustment (section 3.4.3 in Tsujino et al., 2018) is recommended here.

## Declaration of competing interest

The authors declare that they have no known competing financial interests or personal relationships that could have appeared to influence the work reported in this paper.

## Acknowledgments

We gratefully thank Dr. Keith Lindsay (NCAR) for his suggestions and help in conducting three experiments using CESM in this study. We also gratefully thank Jianhua Lu (SYSU) for thorough comments and suggestions on the manuscript. Drs. Sun, Liu and Lin are supported by the National Natural Science Foundation of China (Grants 41931183 and 41776030) and the National Key Scientific and Technological Infrastructure, China project “Earth System Science Numerical Simulator Facility” (EarthLab). Dr. Tseng is supported by the MOST106-2111-M-002-001 “Development and Validation of a New-generation, Fully-Coupled Global Climate System Model”, Taiwan. Dr. Small was supported by the NSF Earth System Model (EaSM), USA Grant 1419292. Dr. Bryan is supported by National Science Foundation, USA through its sponsorship of NCAR. The code of CESM2 can be downloaded from [http://www.cesm.ucar.edu/models/cesm2/release\\_download.html](http://www.cesm.ucar.edu/models/cesm2/release_download.html). The model data used in this paper can be downloaded from <https://pan.baidu.com/disk/home?#/all?vmode=list&path=%2Fdata%20for%20AGU%202020>.

## Appendix A. Supplementary data

Supplementary material related to this article can be found online at <https://doi.org/10.1016/j.ocemod.2021.101876>.

## References

Belmonte Rivas, M., Stoffelen, A., 2019. Characterizing ERA-Interim and ERA5 surface wind biases using ASCAT. *Ocean Sci.* 15 (3), 831–852.

Bentamy, A., Grodsky, S.A., Carton, J.A., Croizé-Fillon, D., Chapron, B., 2012. Matching ASCAT and QuikSCAT winds. *J. Geophys. Res. Oceans* 117 (C2).

Chelton, D.B., Esbensen, S.K., Schlax, M.G., Thum, N., Freilich, M.H., Wentz, F.J., et al., 2001. Observations of coupling between surface wind stress and sea surface temperature in the eastern tropical pacific. *J. Clim.* 14 (7), 1479–1498. [http://dx.doi.org/10.1175/1520-0442\(2001\)014.2.0.CO;2](http://dx.doi.org/10.1175/1520-0442(2001)014.2.0.CO;2).

Chelton, Dudley, Schlax, M.G., Freilich, M.H., Milliff, R.F., 2004. Satellite measurements reveal persistent small-scale features in ocean winds. *Science* 303 (978), <http://dx.doi.org/10.1126/science.1091901>.

Chen, Y., Fu, Y., 2017. Characteristics of VIRS signals within pixels of TRMM PR for warm rain in the tropics and subtropics. *J. Appl. Meteorol. Climatol.* 56 (3), 789–801. <http://dx.doi.org/10.1175/JAMC-D-16-0198.1>.

Chen, X., Qiu, B., Du, Y., Chen, S., Qi, Y., 2016. Interannual and interdecadal variability of the North Equatorial Countercurrent in the Western Pacific. *J. Geophys. Res. Oceans* 121, 7743–7758. <http://dx.doi.org/10.1002/2016JC012190>.

Clement, A.C., Seager, R., Murtugudde, R., 2005. Why are the tropical warm pool? *J. Clim.* 18, 5294–5311. <http://dx.doi.org/10.1175/JCLI3582.1>.

Cornillon, P., Park, K.A., 2002. Warm core ring velocities inferred from NSCAT. *Geophys. Res. Lett.* 28 (4), 575–578. <http://dx.doi.org/10.1029/2000GL011487>.

Danabasoglu, G., Yeager, S.G., Bailey, D., et al., 2014. North atlantic simulations in coordinated ocean-ice reference experiments phase II (CORE-II). Part I: Mean states. *Ocean Model.* 73 (1), 76–107.

Donguy, J.R., Meyers, G., 1996. Mean annual variation of transport of major currents in the tropical Pacific Ocean. *Deep-Sea Res. I* 43 (7), 0–1122. [http://dx.doi.org/10.1016/0967-0637\(96\)00047-7](http://dx.doi.org/10.1016/0967-0637(96)00047-7).

Giese, B.S., Ray, S., 2011. El Niño variability in simple ocean data assimilation (SODA), 1871–2008. *J. Geophys. Res. Oceans* 116.

Hersbach, H., Bidlot, J.-R., 2008. The relevance of ocean surface current in the ECMWF analysis and forecast system. In: *Workshop on Ocean-Atmosphere Interaction*. pp. 61–73.

JMA, 2013. Outline of the Operational Numerical Weather Prediction at the Japan Meteorological Agency. URL: <https://www.jma.go.jp/jma/jma-eng/jma-center/nwp/outline2013-nwp/index.htm>.

Johnson, Eric S., Bonjean, Fabrice, Lagerloef, Gary S.E., Gunn, John T., Mitchum, G.T., 2007. Validation and error analysis of OSCAR sea surface currents. *J. Atmos. Ocean. Technol.* 24 (24), 688–701.

Johnson, G.C., Sloyan, B.M., Kessler, W.S., McTaggart, K.E., 2002. Direct measurements of upper ocean currents and water properties across the tropical Pacific during the 1990s. *Prog. Oceanogr.* 52 (1), 31–61. [http://dx.doi.org/10.1016/S0079-6611\(02\)00021-6](http://dx.doi.org/10.1016/S0079-6611(02)00021-6).

Jullien, S., Masson, S., Oerder, V., Samson, G., Colas, F., Renault, L., 2020. Impact of ocean-atmosphere current feedback on ocean mesoscale activity: Regional variations and sensitivity to model resolution. *J. Clim.* 33 (7), 2585–2602.

Kelly, K.A., Dickinson, S., McPhaden, M.J., Johnson, G.C., 2001. Ocean currents evident in satellite wind data. *Geophys. Res. Lett.* 28 (28), 2469–2472.

Kessler, W.S., Johnson, G.C., Moore, D.W., 2003. Sverdrup and nonlinear dynamics of the Pacific equatorial currents. *J. Phys. Oceanogr.* 33 (5), 994–1008. [http://dx.doi.org/10.1175/1520-0485\(2003\)033.2.0.CO;2](http://dx.doi.org/10.1175/1520-0485(2003)033.2.0.CO;2).

Kilpatrick, T.J., Xie, S.P., 2016. Circumventing rain-related errors in scatterometer wind observations. *J. Geophys. Res.: Atmos.*

King, G.P., Portabella, M., Lin, W., Stoffelen, A., 2017. Correlating extremes in wind and stress divergence with extremes in rain over the Tropical Atlantic.

de Kloe, J., Stoffelen, A., Verhoef, A., 2017. Improved use of scatterometer measurements by using stress-equivalent reference winds. *IEEE J. Sel. Top. Appl. Earth Obs. Remote Sens.* 10 (5), 2340–2347.

Large, W.G., Yeager, S.G., 2004. Diurnal to Decadal Global Forcing for Ocean and Sea-Ice Models: The Data Sets and Flux Climatologies. NCAR Technical Note NCAR/TN-460+STR, <http://dx.doi.org/10.5065/D6KK98Q6>.

Large, W.G., Yeager, S.G., 2009. The global climatology of an interannually varying air-sea flux data set. *Clim. Dynam.* 33 (2–3), 341–364. <http://dx.doi.org/10.1007/s00382-008-0441-3>.

Liu, W.T., Tang, W., 1996. Equivalent Neutral Wind. *JPL Publication 96-17*, Jet Propulsion Laboratory, Pasadena, p. 16.

Masunaga, H., L'Ecuyer, T.S., 2011. Equatorial asymmetry of the East Pacific ITCZ: Observational constraints on the underlying processes. *J. Clim.* 24 (6), 1784–1800. <http://dx.doi.org/10.1175/2010JCLI3854.1>.

Meyers, G., Donguy, J.R., 1984. The North Equatorial Countercurrent and heat storage in the western Pacific Ocean during 1982–83. *Nature* 312 (5991), 258. <http://dx.doi.org/10.1038/312258a0-260>.

Milliff, R.F., Morzel, J., Chelton, D.B., et al., 2004. Wind stress curl and wind stress divergence biases from rain effects on QSCAT surface wind retrievals. *J. Atmos. Ocean. Technol.* 21 (8), 1216–1231.

O'Neill, L.W., Haack, T., Durland, T., 2015. Estimation of time-averaged surface divergence and vorticity from satellite ocean vector winds. *J. Clim.* 28 (19), 7596–7620. <http://dx.doi.org/10.1175/JCLI-D-15-0119.1>.

Picaut, J., Delcroix, T., 1995. Equatorial wave sequence associated with warm pool displacement during the 1986-1989 El Ni~no-LaNi~na. *J. Geophys. Res.* 100, 18, 393–18, 408. [http://dx.doi.org/10.1175/1520-0426\(2001\)018<1171:RDAQCO>2.0.CO;2](http://dx.doi.org/10.1175/1520-0426(2001)018<1171:RDAQCO>2.0.CO;2).

Renault, L., Masson, S., Arsouze, T., et al., 2020. Recipes for how to force oceanic model dynamics. *J. Adv. Modelling Earth Syst.* 12 (2).

Reynolds, R.W., Smith, T.M., Liu, C., Chelton, D.B., Casey, K.S., Schlax, M.G., 2007. Daily high-resolution-blended analyses for sea surface temperature. *J. Clim.* 20, 5473–5496. <http://dx.doi.org/10.1175/JCLI-D-14-00293.1>.

Ricciardulli, L., Wentz, F.J., 2015. A scatterometer geophysical model function for climate-quality winds: QuikSCAT Ku-2011. *J. Atmos. Ocean. Technol.* 32 (10), 1829–1846.

Richards, Kelvin, et al., 2009. Vertical mixing in the ocean and its impact on the coupled ocean/atmosphere system in the Eastern Tropical Pacific. *J. Clim.* 22 (13), 3703–3719. <http://dx.doi.org/10.1175/2009JCLI2702.1>.

Risien, C.M., Chelton, D.B., 2008. A global climatology of surface wind and wind stress fields from eight years of QuikSCAT scatterometer data. *J. Phys. Oceanogr.* 38 (11), 2379–2413.

Schmidtko, S., Johnson, G.C., Lyman, J.M., MIMOC, 2013. A global monthly isopycnal upper-ocean climatology with mixed layers. *J. Geophys. Res. Oceans* 118 (4), 1658–1672.

Stoffelen, A., Kumar, R., Zou, J., Karaev, V., Chang, P.S., Rodriguez, E., 2019. Ocean surface vector wind observations. In: *Remote Sensing of the Asian Seas*. Springer, Cham, pp. 429–447.

Sun, Zhikuo, Liu, Hailong, Lin, Pengfei, Tseng, Yu-heng, Bryan, Frank, Small, Justin, 2019. Impacts of ocean-atmospheric interaction on the modelling of NECC. *J. Adv. Modelling Earth Syst.* <http://dx.doi.org/10.1029/2018MS001521>.

Tan, S., Zhou, H., 2018. The observed impacts of the two types of El Ni~o on the North Equatorial Countercurrent in the Pacific Ocean. *Geophys. Res. Lett.* 45, 10, 493–10, 500. <http://dx.doi.org/10.1029/2018GL079273>.

Tseng, Y.H., Lin, H., Chen, H.C., Thompson, K., Bentsen, M., Böning, C.W., et al., 2016. North and equatorial Pacific Ocean circulation in the CORE-II hindcast simulations. *Ocean Model.* 104, 143–170. <http://dx.doi.org/10.1016/j.ocemod.2016.06.003>.

Tsujino, Hiroyuki, et al., 2018. JRA-55 based surface dataset for driving ocean - sea-ice models (JRA55-do). *Ocean Model.* <http://dx.doi.org/10.1016/j.ocemod.2018.07.002>.

Tsujino, H., Urakawa, L., Griffies, S., Danabasoglu, G., Adcroft, A., Amaral, A., Arsouze, T., Bentsen, M., Bernardello, R., Böning, C., Bozec, A., Chassignet, E., Danilov, S., Dussin, R., Exarchou, E., Fogli, P., Fox-Kemper, B., Guo, C., Ilicak, M., Iovino, D., Kim, W., Koldunov, N., Lapin, V., Li, Y., Lin, P., Lindsay, K., Liu, H., Long, M., Komuro, Y., Marsland, S., Masina, S., Nummelin, A., Rieck, J., Ruprich-Robert, Y., Scheinert, M., Sicardi, V., Sidorenko, D., Suzuki, T., Tatebe, H., Wang, Q., Yeager, S., Yu, Z., 2020. Evaluation of global ocean-sea-ice model simulations based on the experimental protocols of the Ocean Model Intercomparison Project phase 2 (OMIP-2) Geoscientific Model Development Discussions. <http://dx.doi.org/10.5194/gmd-2019-363>.

Wang, Z., Stoffelen, A., Zhang, B., He, Y., Lin, W., Li, X., 2019. Inconsistencies in scatterometer wind products based on ASCAT and OSCAT-2 collocations. *Remote Sens. Environ.* 225, 207–216.

Weissman, D.E., Bourassa, M.A., Tongue, J., 2002. Effects of rain rate and wind magnitude on SeaWinds scatterometer wind speed errors. *J. Atmos. Ocean. Technol.* 19 (5), 738–746.

Wentz, F.J., Smith, D.K., 1999. A model function for the ocean-normalized radar cross section at 14 ghz derived from nscat observations. *J. Geophys. Res. Oceans* 104 (C5), 11499–11514. <http://dx.doi.org/10.1029/98JC02148>.

Wu, F., Lin, P., Liu, H., 2012. Influence of a southern shift of the ITCZ from quick scatterometer data on the Pacific North Equatorial Countercurrent. *Adv. Atmos. Sci.* 29 (6), 1292–1304. <http://dx.doi.org/10.1007/s00376-012-1149-1>.

Wyrski, K., Kendall, R., 1967. Transports of the Pacific Equatorial Countercurrent. *J. Geophys. Res.* 72 (8), 2073–2076. <http://dx.doi.org/10.1029/JZ072i008p02073>.

Xu, X., Stoffelen, A., 2020. Improved rain screening for Ku-Band wind scatterometry. *IEEE Trans. Geosci. Remote Sens.* 58 (4), 2494–2503. <http://dx.doi.org/10.1109/TGRS.2019.2951726>.